Journal of Biomedical Optics

BiomedicalOptics.SPIEDigitalLibrary.org

High-throughput ultraviolet photoacoustic microscopy with multifocal excitation

Toru Imai
Junhui Shi
Terence T. W. Wong
Lei Li
Liren Zhu
Lihong V. Wang

SPIE.

Toru Imai, Junhui Shi, Terence T. W. Wong, Lei Li, Liren Zhu, Lihong V. Wang, "High-throughput ultraviolet photoacoustic microscopy with multifocal excitation," *J. Biomed. Opt.* **23**(3), 036007 (2018), doi: 10.1117/1.JBO.23.3.036007.

High-throughput ultraviolet photoacoustic microscopy with multifocal excitation

Toru Imai,[a,b] Junhui Shi,[a] Terence T. W. Wong,[a,b] Lei Li,[a] Liren Zhu,[a,b] and Lihong V. Wang[a,*]
[a]California Institute of Technology, Caltech Optical Imaging Laboratory, Andrew and Peggy Cherng Department of Medical Engineering, Department of Electrical Engineering, Pasadena, California, United States
[b]Washington University in St. Louis, Department of Biomedical Engineering, St. Louis, Missouri, United States

Abstract. Ultraviolet photoacoustic microscopy (UV-PAM) is a promising intraoperative tool for surgical margin assessment (SMA), one that can provide label-free histology-like images with high resolution. In this study, using a microlens array and a one-dimensional (1-D) array ultrasonic transducer, we developed a high-throughput multifocal UV-PAM (MF-UV-PAM). Our new system achieved a 1.6 ± 0.2 μm lateral resolution and produced images 40 times faster than the previously developed point-by-point scanning UV-PAM. MF-UV-PAM provided a readily comprehensible photoacoustic image of a mouse brain slice with specific absorption contrast in ~16 min, highlighting cell nuclei. Individual cell nuclei could be clearly resolved, showing its practical potential for intraoperative SMA. [DOI: 10.1117/1.JBO.23.3.036007]

Keywords: photoacoustic imaging; ultraviolet laser; surgical margin assessment; microlens array; 1-D array ultrasonic transducer.
Paper 170796R received Dec. 8, 2017; accepted for publication Feb. 22, 2018; published online Mar. 15, 2018.

1 Introduction

Surgical margin assessment (SMA) is considered to play a significant role in reducing the local recurrence rate of a variety of cancer types.[1–7] In the histological analysis performed for SMA, morphological features of cell nuclei provide critical information to identify cancer cells through microscopic examination.[8,9] Currently, postoperative histological analysis of excised and stained specimens is widely performed and regarded as the standard procedure. However, this analysis typically includes laborious and time-consuming processes before imaging, such as tissue processing, embedding, sectioning, and staining. Comprehensive initial detection is another concern. In the case of breast conserving surgery, for instance, over 20% of patients are required to have a second surgery based on the results of postoperative analysis.[10–18] Clearly, this undesirable re-excision surgery adversely affects the patients' quality of life by increasing health care costs, adding physical and psychological burdens, and potentially delaying adjuvant therapy. To avoid re-excision surgeries, an intraoperative SMA as reliable as the conventional postoperative SMA has been highly sought. One rapid sectioning technique, frozen sectioning along with staining, can be performed intraoperatively. However, this technique has not been widely used, mainly due to the technical difficulty of freezing adipose-rich tissue, including breast tissue, and the low quality of slices compared with those obtained from a conventional sectioning method, such as paraffin-embedding sectioning.[19,20] Another, more recent option for rapid histological analysis, microscopy with ultraviolet surface excitation (MUSE), requires only a brief staining time and inexpensive excitation light source and can image specimens without tissue sectioning.[21,22] However, MUSE can provide only superficial images of specimens, less than 10 μm below the surface,[22] and, based on current SMA criteria, such a thin examined layer may be inadequate to secure a low local recurrence rate of cancer.[1,7] Other than histological methods requiring staining, several label-free optical imaging techniques can be performed intraoperatively, including reflectance confocal microscopy,[23–25] third-harmonic generation microscopy,[26,27] multiphoton autofluorescence microscopy,[28,29] and stimulated Raman scattering microscopy.[30] The contrast of reflectance confocal microscopy relies on the refractive index, which is not specific to the cell nucleus; thus, a comparable background signal can hamper a reliable SMA. The same nonspecific contrast issue confronts third-harmonic generation microscopy as well. Multiphoton autofluorescence microscopy currently can provide only a negative contrast of DNA/RNA, making it innately challenging to confirm the present or exact shape of a nucleus. Stimulated Raman scattering microscopy can provide contrast-specific imaging of the cell nuclei by spectral decomposition. However, when the typical rough surface of an excised specimen is to be imaged without tissue sectioning, due to its few-micrometers depth of focus, stimulated Raman scattering microscopy may need multiple scanning sessions, shifting the focal plane along the depth direction for each session, to acquire a complete surface image of the specimen. To address all of these challenges, in previous studies, our lab developed ultraviolet photoacoustic microscopy (UV-PAM), which provides label-free and high contrast images of DNA/RNA in cell nuclei with greater imaging depth than a conventional histological image.[31–34] UV light absorption at 266 nm by DNA/RNA is an order of magnitude higher than that by other biomolecules, such as lipids or proteins.[31,32] We demonstrated that UV-PAM was able to provide analysis of the same quality as postoperative histological analysis and that it required less time.[33] This demonstration suggested that UV-PAM could potentially provide accurate intraoperative SMA, reducing the rate of re-excision in cancer surgeries. Further technical advances in UV-PAM can help this technology achieve its full potential. The most sought-after improvement is the imaging

*Address all correspondence to: Lihong V. Wang, E-mail: LVW@caltech.edu

1083-3668/2018/$25.00 © 2018 SPIE

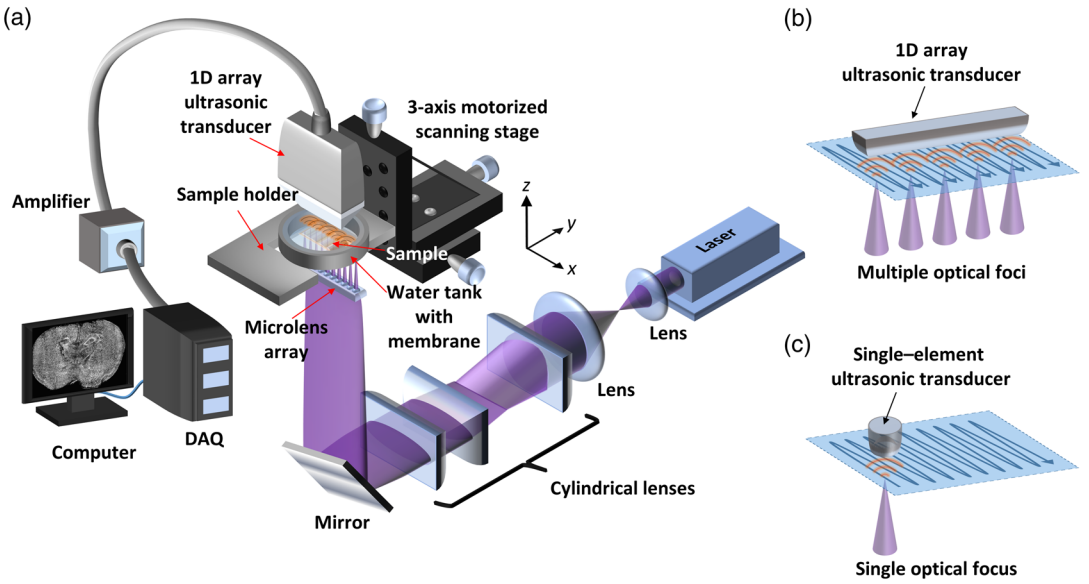

Fig. 1 Schematic of multifocal ultraviolet laser photoacoustic microscopy (MF-UV-PAM) system and a comparison with conventional ultraviolet laser photoacoustic microscopy (UV-PAM). (a) Schematic of MF-UV-PAM. (b) The conventional UV-PAM system with a single optical focal point. (c) MF-UV-PAM system with multiple optical focal points.

speed. The current UV-PAM system acquires photoacoustic (PA) signals on a point-by-point basis with raster scanning, so its imaging speed is limited by the repetition rate of the laser, a critical bottleneck to practical clinical applications such as intraoperative SMA.[33]

In this study, we developed a multifocal UV-PAM (MF-UV-PAM) system to mitigate this limitation. By exciting the biological specimens with multiple optical spots, and subsequently reconstructing the induced PA signals at these points, imaging can be accelerated by increasing the number of excitation foci.[35–37] Thus, the imaging speed can be improved drastically without being solely limited by the laser repetition rate, while the lateral resolution remains optically defined.

2 Methods and Materials

2.1 *Multifocal UV-PAM System*

Based on the PA phenomenon, our MF-UV-PAM system [Fig. 1(a)] produced PA images by detecting acoustic waves generated using UV light. A nanosecond pulsed UV laser (266-nm wavelength, 10-kHz laser repetition rate; WEDGE HF 266 nm, Bright Solutions Srl.) was employed for PA excitation. The laser beam diameter was first expanded by a set of lenses (LA4647 and LA4663, Thorlabs Inc.). The laser beam width in one direction was then reduced by a set of cylindrical lenses (LJ4709RM and LJ4281RM, Thorlabs Inc.), which was followed by converging the width further by another cylindrical lens (LJ4147RM, Thorlabs Inc.) to illuminate a one-dimensional (1-D) microlens array [250-μm lens pitch, 835-μm radius of curvature, 40 micro lenses, 0.075 numerical aperture (NA); SUSS Microtec Se.]. By means of the 1-D microlens array, the laser beam was transformed into multifocal spots focused on the bottom side of an imaging sample, which was placed on the bottom of a water tank filled with water. Part of the generated acoustic waves propagated inside the sample and water and then were detected by a focused 1-D array ultrasonic transducer (50-MHz center frequency, 256 elements; MS 700, FUJIFILM VisualSonics, Inc.). The received acoustic pressure was converted to an electric signal, amplified, and sent to a 256-channel data acquisition system (DAQ), which consisted of two PXIe-1085 chassis managed by PXIe-8880 controllers (National Instruments), each configured with 16 PXIe-5170R data acquisition boards. The DAQ digitalized the 256-channel amplified signals at 250 MS/s and then transferred the data to a computer for recording. In the computer, using MATLAB (Mathworks, Inc.),[38] the PA image was reconstructed based on the recorded signals and, finally, was displayed on a screen. Cross-sectional images or volumetric images could be produced, respectively, by linear or raster scanning of the sample using a motorized scanning stage. The stage scanning, data acquisition trigger, and laser emission were all synchronized by a microcontroller (Mega 2560, Arduino), and the control interface was programmed in LabVIEW (National Instruments).

2.2 *Image Reconstruction*

Image reconstruction was performed using the universal back projection (UBP) algorithm.[39] With UBP, the lateral resolution of the reconstructed image was first determined acoustically, based on the specification of the 1-D array ultrasonic transducer, which was 75 μm. Then, based on the locations of the multifocal spots, which were known a priori from a reference sample with spatially uniform light absorption, the locations of the reconstructed image at the multifocal spots were optically determined. By repeating the image reconstruction based on PA signals acquired at different locations, cross-sectional images or volumetric images were able to be acquired. Because MF-UV-PAM can simultaneously acquire the PA signals needed to reconstruct the PA image at multiple locations [Fig. 1(b)], the required scanning area per optical focal point was smaller than that for the previous UV-PAM, which had only a single objective and a single-element ultrasonic transducer [Fig. 1(c)]. Thus, the imaging speed could be multiplied by the number of the focal spots, or by 40 times with the microlens array employed in the current system.

2.3 *System Performance Evaluation*

To evaluate the lateral and axial resolutions of the system, gold nanoparticles (100 nm diameter; 753688-25ML, Sigma-Aldrich Co, LLC) were imaged in 0.300 μm steps in the X dimension and 0.313 μm steps in the Y dimension (the slight difference in step sizes was an incidental result of the drivers used). The gold nanoparticles were placed on the polyethylene membrane of the water tank and dried. Then, to prevent them from being detached from the membrane while imaging, low gelling temperature agarose (A9414-100G, Sigma-Aldrich Co, LLC) was placed on top. To evaluate the lateral resolution, after reconstructing the PA image of a single gold nanoparticle, its maximum amplitude projection (MAP), a projection onto the XY plane [Fig. 1(a)] of the peak-to-peak value along the depth direction [Z direction in Fig. 1(a)], was fitted with a two-dimensional (2-D) isotropic Gaussian curve. Then the full width at half maximum (FWHM) of the point spread function (PSF) was calculated. To evaluate the axial resolution, the envelope of the curve of the reconstructed 1-D image along the depth direction of the PA signal was first extracted using the Hilbert transformation, and then the FWHM was calculated. To demonstrate the system's capability to acquire depth information, we imaged crossed hairs with diameters of around 100 μm. They were located spatially apart in the depth direction with the distance of their diameter.

2.4 *Biological Sample Imaging*

To demonstrate the system's capability to image biological samples, a fixed mouse's brain slice was imaged. The protocol was approved by the Institutional Review Board at the California Institute of Technology. To prepare this sample, the mouse brain was first dissected out, fixed with formalin, and sliced by a vibratome to a thickness of around 200 μm. For imaging, the formalin-fixed brain slice was placed at the bottom of the water tank and secured by sandwiching it between two polyethylene film membranes. To acquire an image of the whole area (10.5 mm × 10.0 mm) of the sliced sample, due to the limitation of the current buffer memory of the DAQ, we conducted eight separate imaging sessions. For each session, the field of view was 1.4 mm × 10.0 mm, and the imaging time was around 2 min, with a 1.00 μm × 1.25 μm step size. To stitch each image into the final whole image, the neighboring images have a partial overlap area of 0.1 mm × 10.0 mm at their edges. Each area was scanned so that the fast scanning axis was along the 1.4 mm side, and the slow scanning axis was perpendicular to the fast scanning axis, whose 250 μm length was the pitch size of the 1-D microlens array. Even though we used a sectioned and formalin-fixed sample in this imaging, a freshly dissected and unprocessed biological sample could be imaged with our system as quickly as with our previous UV-PAM system.[33]

3 Results

3.1 *System Performance*

Figure 2(a) shows a representative result of the PA MAP image of a gold nanoparticle, and Fig. 2(b) shows the same PA MAP data with isotropic 2-D Gaussian fitting in a 3-D rendering, with its z-axis as the normalized PA amplitude. The calculated mean value of the FWHM of the lateral PSF was 1.6 ± 0.2 μm (mean value ± standard deviation, 10 samples), which was

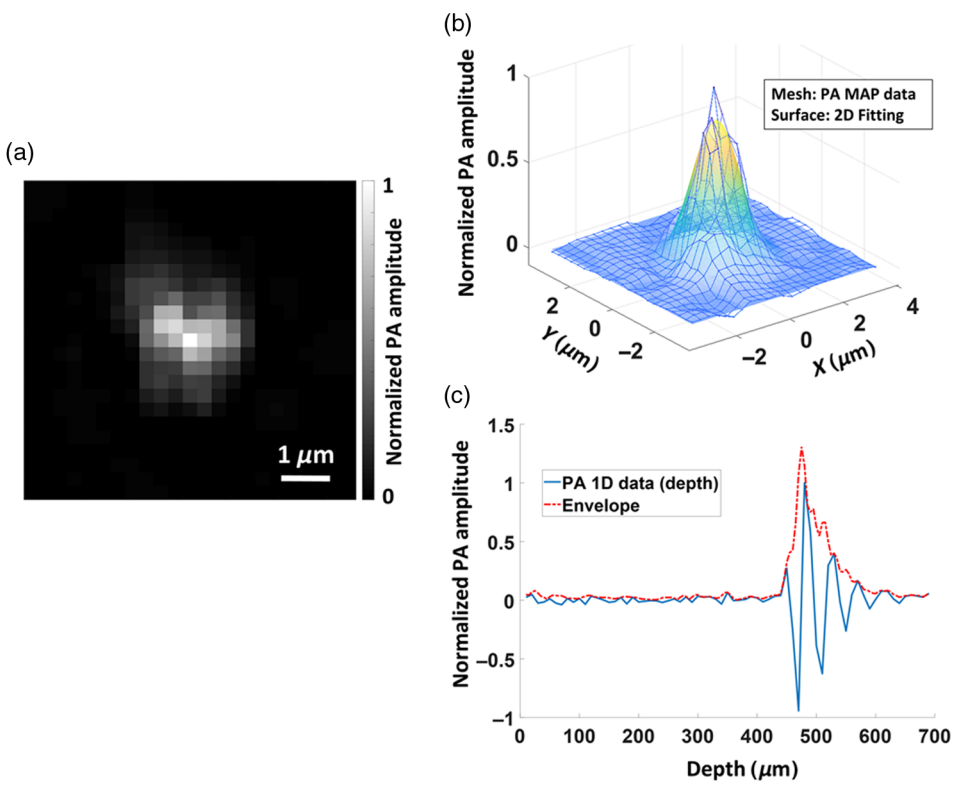

Fig. 2 Lateral and axial resolutions of the MF-UV-PAM system. (a) A representative MAP image of the photoacoustic signal of a gold nanoparticle. (b) Isotropic 2-D Gaussian fitting of the MAP image in (a). (c) Reconstructed 1-D image along the depth direction of the gold nanoparticle in (a) and its Hilbert transformation.

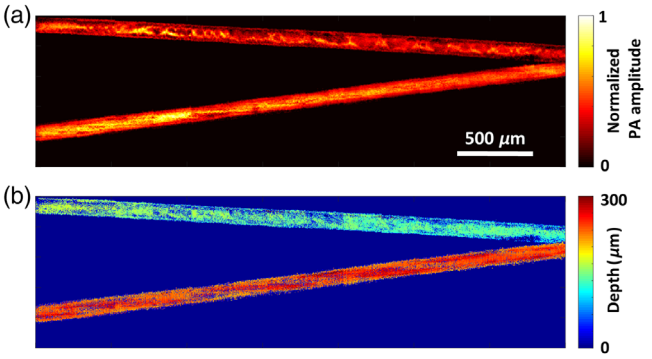

Fig. 3 MAP image of the PA signal and 2-D depth information of crossed hairs located at different depths. (a) PA MAP image and (b) 2-D depth information.

reasonably close to the theoretical value, 1.8 μm $\lambda/2$NA, where λ is the wavelength of the laser beam. Figure 2(c) shows a reconstructed 1-D image along the depth direction of the gold nanoparticle in Fig. 2(a) and the absolute value of its Hilbert transform (envelope of the curve). The calculated mean value of FWHM of the axial PSF was 40.9 ± 6.9 μm (10 samples). Figure 3(a) shows the PA MAP image of the crossing hairs in the clear medium, and Fig. 3(b) shows the corresponding 2-D depth information of each hair, which shows that the hairs located at different depths can be clearly distinguished.

3.2 *Mouse Brain Slice Imaging*

Figure 4(a) shows a PA MAP image of a coronal section of the fixed mouse's brain. The total scanning time of this image was around 16 min, which was 40 times faster than possible with the older imaging system using a single-element ultrasonic transducer and a stepping motor for scanning. Figures 4(b)–4(d) show close-up images of the hippocampal region, the olfactory region, and the retrosplenial region of the cerebral neocortex in Fig. 4(a), respectively. Even in the dense region of the nuclei, the individual nuclei are clearly differentiated. Figure 4(e) shows a representative PA MAP image of a single nucleus with diameter of around 5 μm, from Fig. 4(d).

4 Discussion

Compared with the earlier UV-PAM employing a single objective, the lateral resolution of the MF-UV-PAM is generally degraded by a few times because the NA of the commercially sourced microlens array is smaller than that of commercially available single objectives. However, the lateral resolution achieved in this study could sufficiently differentiate individual cell nuclei. To further improve the performance of MF-UV-PAM for SMA, it is more important to improve the axial resolution, in other words, to achieve optical sectioning capability. Several techniques have been developed previously, including a technique utilizing Grüneisen relaxation,[40] extracting the higher orders of the PA signal,[41] or utilizing multiview excitation.[42] Providing high lateral and axial resolutions can reduce false-positive margins[33] as well as provide information about intranuclear structures, which may prove useful in achieving a more accurate SMA.

To increase the imaging speed further, we can use a microlens array with an even higher microlens density within the same size. A limiting factor capping this density is the acoustically determined lateral resolution of the 1-D array ultrasonic transducer, 75 μm in our system. If the microlens density is so high that the distance between the neighboring microlenses is comparable to or smaller than this lateral resolution, the reconstructed images of the neighboring focal spots will start to overlap, and the neighboring signals will affect each other (cross-talk). In our system, to guarantee the image quality by minimizing cross-talk, we used a microlens array with a pitch of 250 μm. However, a microlens array with a smaller pitch could possibly be used if the pitch is above the limiting factor. The maximum number of the available microlenses is also limited. Due to the limitation of the available laser energy, as the number of the microlens increases, the laser energy available for a single microlens decreases; thus, the SNR also decreases accordingly. Assuming that the SNR is proportional to the laser energy per single microlens and a cell nucleus image with an SNR of 5 provides adequate quality for SMA, then, given the SNR of 73.6 for a single nucleus in our system [Fig. 4(e)], the maximum possible number of microlenses would be 588 using a laser with the same total energy. In designing a real system under the two limiting factors above, if we employ a 1-D microlens array with the smallest possible pitch, the maximum number of microlenses would be only 133. However, we can also consider a system using a 2-D microlens array with a 1-D array ultrasonic transducer. A 2-D PA image can be reconstructed if the PA sources produced at the multiple points illuminated by the 2-D microlens array are located within the acoustically sensitive area of the 1-D array ultrasonic transducer. This configuration can be achieved with side detection of the PA signal by the 1-D array ultrasonic transducer. Because the acoustically sensitive area of

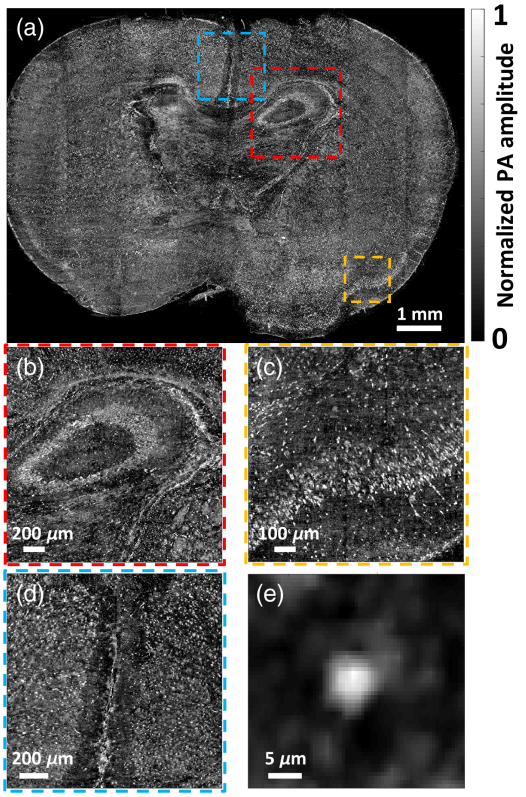

Fig. 4 MAP image of the PA signal of a fixed mouse's brain slice: (a) PA MAP image of the whole area of the brain slice; (b) close-up image of the hippocampal region; (c) close-up image of the olfactory region; (d) close-up image of the retrosplenial region of the cerebral neocortex; and (e) close-up image of a single nucleus.

our 1-D array, ultrasonic transducer is around 7 mm (depth direction) by 10 mm (lateral direction), 588 microlenses are easily accommodated, even with a 250 μm pitch 2-D microlens array. Accordingly, the imaging speed can be improved in proportion to the number of microlenses. In addition, if a high energy laser and/or a 1-D array ultrasonic transducer with a higher acoustic resolution is available in the future, more microlenses could be employed to improve the imaging speed.

Based on our estimate, instead of using the microlens array, simply replacing the motorized stage with a fast scanning device, such as a galvo-mirror, MEMS mirror, or voice-coil motor, would improve the imaging speed by around two to four times at best. This improved speed, however, is considered not to be significantly better than that of our proposed method, and is not sufficient for intraoperative SMA. However, in future studies that employ a laser operating at a higher repetition rate beyond the maximum response speed of the motorized stage, integrating a fast scanning device into the system would help to maximize the imaging speed. Such an integration could be readily implemented for our MF-UV-PAM.

Last, we should consider the possibility of revising the current transmission-mode setup to enable *in vivo* imaging, including reflection-mode imaging. The simplest way would be to place the 1-D array ultrasonic transducer at the same side of the 1-D microlens array, but at a tilted angle to make sufficient space to place the 1-D microlens array right above/below the sample. As in our current setup, the tilted 1-D array ultrasonic transducer and the 1-D microlens array must keep the optical focal points and the acoustic focal line confocally aligned. This way, the PA signals excited at the multiple optical spots can be detected by the 1-D focused ultrasonic transducer. In implementing the system in reality, we will have to optimize the space carefully so that the 1-D array ultrasonic transducer does not interfere with the microlens array. Also, the optimal tilt angle of the 1-D array ultrasonic transducer needs to be carefully investigated to achieve sufficient acoustic sensitivity. Instead of tilting only the 1-D array ultrasonic transducer, we could tilt the optical axis of the microlens array, or we could tilt both. Second, we can use a 2-D microlens array and a ring-shaped or 1-D array ultrasonic transducer. The combination of a 2-D microlens array and a ring-shaped array ultrasonic transducer would be similar to the design used in a previous study by our lab.[35] This design may not be categorized as reflection-mode; however, an intact live animal can be placed under the 2-D microlens array with no need for slicing, enabling *in vivo* imaging. A combination of a 2-D microlens array and a 1-D array ultrasonic transducer would basically follow the same configuration as discussed above in estimating the maximum possible number of microlenses. This configuration could be potentially used for *in vivo* imaging as well.

In summary, we demonstrated that UV-PAM employing a 1-D microlens array and 1-D array ultrasonic transducer can successfully achieve an imaging throughput several tens of times higher than that of the conventional point-by-point scanning method, while keeping satisfactory image quality. This demonstration is an important milestone for the practical implementation of UV-PAM for intraoperative SMA.

Disclosures

L.V.W. has financial interests in Microphotoacoustics, Inc., CalPACT, LLC, and Union Photoacoustic Technologies, Ltd., which, however, did not support this work.

Acknowledgments

The authors appreciate the close reading of the manuscript by Prof. James Ballard. This work was sponsored by National Institutes of Health (NIH) Grants R01 CA186567 (NIH Director's Transformative Research Award), U01 NS090579 (NIH BRAIN Initiative), U01 NS099717 (NIH BRAIN Initiative), and R01 EB016963, and supported in part by the March of Dimes Prematurity Research Center.

References

1. B. Sigal-Zafrani et al., "Histological margin assessment for breast ductal carcinoma in situ: precision and implications," *Mod. Pathol.* **17**(1), 81–88 (2004).
2. W. Sienel et al., "Frequency of local recurrence following segmentectomy of stage IA non-small cell lung cancer is influenced by segment locatisation and width of resection margins—implications for patient selection for segmentectomy," *Eur. J. Cardio-Thorac. Surg.* **31**(3), 522–528 (2007).
3. S. B. Ravi and S. Annavajjula, "Surgical margins and its evaluation in oral cancer: a review," *J. Clin. Diagn. Res.* **8**(9), ZE01–ZE05 (2014).
4. J. P. Neoptolemos et al., "Influence of resection margins on survival for patients with pancreatic cancer treated by adjuvant chemoradiation and/or chemotherapy in the ESPAC-1 randomized controlled trial," *Ann. Surg.* **234**(6), 758–768 (2001).
5. F. Meric et al., "Positive surgical margins and ipsilateral breast tumor recurrence predict disease-specific survival after breast-conserving therapy," *Cancer* **97**(4), 926–933 (2003).
6. J. Figueras et al., "Effect of subcentimeter nonpositive resection margin on hepatic recurrence in patients undergoing hepatectomy for colorectal liver metastases. Evidences from 663 liver resections," *Ann. Oncol.* **18**(7), 1190–1195 (2007).
7. M. S. Moran et al., "Society of surgical oncology—American Society for Radiation Oncology consensus guideline on margins for breast-conserving surgery with whole-breast irradiation in stages I and II invasive breast cancer," *J. Clin. Oncol.* **32**(14), 1507–1515 (2014).
8. D. Zink, A. H. Fischer, and J. A. Nickerson, "Nuclear structure in cancer cells," *Nat. Rev. Cancer* **4**(9), 677–687 (2004).
9. L. D. True and C. D. Jordan, "The cancer nuclear microenvironment: interface between light microscopic cytology and molecular phenotype," *J. Cell. Biochem.* **104**(6), 1994–2003 (2008).
10. L. E. McCahill et al., "Variability in reexcision following breast conservation surgery," *J. Am. Med. Assoc.* **307**(5), 467–475 (2012).
11. M. Clarke et al., "Effects of radiotherapy and of differences in the extent of surgery for early breast cancer on local recurrence and 15-year survival: an overview of the randomised trials," *Lancet* **366**(9503), 2087–2106 (2005).
12. R. Jeevan et al., "Reoperation rates after breast conserving surgery for breast cancer among women in England: retrospective study of hospital episode statistics," *Br. Med. J.* **345**, e4505 (2012).
13. L. Jacobs, "Positive margins: the challenge continues for breast surgeons," *Ann. Surg. Oncol.* **15**(5), 1271–1272 (2008).
14. M. C. Lee et al., "Determinants of breast conservation rates: reasons for mastectomy at a comprehensive cancer center," *Breast J.* **15**(1), 34–40 (2009).
15. W. Jung et al., "Factors associated with re-excision after breast-conserving surgery for early-stage breast cancer," *J. Breast Cancer* **15**(4), 412–419 (2012).
16. G. C. Balch et al., "Accuracy of intraoperative gross examination of surgical margin status in women undergoing partial mastectomy for breast malignancy," *Am. Surg.* **71**, 22–28 (2005).
17. T. L. Huston et al., "The influence of additional surgical margins on the total specimen volume excised and the reoperative rate after breast-conserving surgery," *Am. J. Surg.* **192**(4), 509–512 (2006).
18. A. Kobbermann et al., "Impact of routine cavity shave margins on breast cancer re-excision rates," *Ann. Surg. Oncol.* **18**(5), 1349–1355 (2011).
19. F. H. Barakat, I. Sulaiman, and M. A. Sughayer, "Reliability of frozen section in breast sentinel lymph node examination," *Breast Cancer* **21**, 576–582 (2014).

20. V. Rastogi et al., "Artefacts: a diagnostic dilemma—a review," *J. Clin. Diagn. Res.* **7**(10), 2408–2413 (2013).
21. F. E. A. Fereidouni, "Microscopy with UV surface excitation (MUSE) for slide-free histology and pathology imaging," *Proc. SPIE* **9318**, 93180F (2015).
22. R. M. Levenson and F. Fereidouni, "MUSE: a new, fast, simple microscopy method for slide-free histology and surface topography," *FASEB J.* **30** (2016).
23. W. M. White et al., "Noninvasive imaging of human oral mucosa in vivo by confocal reflectance microscopy," *Laryngoscope* **109**(10), 1709–1717 (1999).
24. K. S. Nehal, D. Gareau, and M. Rajadhyaksha, "Skin imaging with reflectance confocal microscopy," *Semin. Cutan. Med. Surg.* **27**(1), 37–43 (2008).
25. S. Gonzalez and Z. Tannous, "Real-time, *in vivo* confocal reflectance microscopy of basal cell carcinoma," *J. Am. Acad. Dermatol.* **47**(6), 869–874 (2002).
26. M. R. Tsai et al., "*In vivo* optical virtual biopsy of human oral mucosa with harmonic generation microscopy," *Biomed. Opt. Express* **2**(8), 2317–2328 (2011).
27. N. V. Kuzmin et al., "Third harmonic generation imaging for fast, label-free pathology of human brain tumors," *Biomed. Opt. Express* **7**(5), 1889–1904 (2016).
28. B. G. Wang, K. Konig, and K. J. Halbhuber, "Two-photon microscopy of deep intravital tissues and its merits in clinical research," *J. Microsc.* **238**(1), 1–20 (2010).
29. C. Q. Li et al., "Multiphoton microscopy of live tissues with ultraviolet autofluorescence," *IEEE J. Sel. Top. Quantum Electron.* **16**(3), 516–523 (2010).
30. D. A. Orringer et al., "Rapid intraoperative histology of unprocessed surgical specimens via fibre-laser-based stimulated Raman scattering microscopy," *Nat. Biomed. Eng.* **1**, 0027 (2017).
31. D. K. Yao et al., "*In vivo* label-free photoacoustic microscopy of cell nuclei by excitation of DNA and RNA," *Opt. Lett.* **35**(24), 4139–4141 (2010).
32. D. K. Yao et al., "Optimal ultraviolet wavelength for in vivo photoacoustic imaging of cell nuclei," *J. Biomed. Opt.* **17**(5), 056004 (2012).
33. T. T. W. Wong et al., "Fast label-free multilayered histology-like imaging of human breast cancer by photoacoustic microscopy," *Sci. Adv.* **3**(5), e1602168 (2017).
34. T. T. W. Wong et al., "Label-free automated three-dimensional imaging of whole organs by microtomy-assisted photoacoustic microscopy," *Nat. Commun.* **8**(1), 1386 (2017).
35. J. Xia et al., "Wide-field two-dimensional multifocal optical-resolution photoacoustic-computed microscopy," *Opt. Lett.* **38**(24), 5236–5239 (2013).
36. L. A. Song, K. Maslov, and L. V. Wang, "Multifocal optical-resolution photoacoustic microscopy in vivo," *Opt. Lett.* **36**(7), 1236–1238 (2011).
37. G. Li, K. I. Maslov, and L. V. Wang, "Reflection-mode multifocal optical-resolution photoacoustic microscopy," *J. Biomed. Opt.* **18**(3), 030501 (2013).
38. P. Zhang et al., "High-resolution deep functional imaging of the whole mouse brain by photoacoustic computed tomography *in vivo*," *J. Biophotonics* **11**, e201700024 (2018).
39. M. Xu and L. V. Wang, "Universal back-projection algorithm for photoacoustic computed tomography," *Phys. Rev. E* **71**(1), 016706 (2005).
40. L. D. Wang, C. Zhang, and L. H. V. Wang, "Grueneisen relaxation photoacoustic microscopy," *Phys. Rev. Lett.* **113**(17), 174301 (2014).
41. A. Danielli et al., "Label-free photoacoustic nanoscopy," *J. Biomed. Opt.* **19**(8), 086006 (2014).
42. L. R. Zhu et al., "Multiview optical resolution photoacoustic microscopy," *Optica* **1**(4), 217–222 (2014).

Toru Imai is a PhD student at Washington University in St. Louis and a visiting special student at the California Institute of Technology. He received his BSc and MSc degrees from Waseda University and is currently an R&D engineer at Canon, Inc. His research interests include developing a photoacoustic microscopy as well as other photoacoustic imaging technologies that can be commercialized in the near future.

Junhui Shi received his BSc degree in chemical physics from the University of Science and Technology of China in 2007. He continued to study chemistry and received his PhD from Princeton University in 2013, for work on theoretical chemical dynamics and experimental nuclear magnetic resonance spectroscopy. Currently, he is working on photoacoustic imaging in the Department of Medical Engineering at the California Institute of Technology.

Terence T. W. Wong is a PhD student at Washington University in St. Louis and a visiting special student at the California Institute of Technology. He received both his BE and MPhil degrees from the University of Hong Kong. His research interests broadly include developing photoacoustic devices to enable label-free and high-speed histology-like imaging and low-cost deep tissue imaging and implementing ultra-fast real-time spectroscopy and microscopy.

Lei Li received his BS and MS degrees from Harbin Institute of Technology, China, in 2010 and 2012, respectively. He is working as a graduate research assistant under the tutelage of Dr. Lihong Wang in the Department of Electrical Engineering, California Institute of Technology. His current research focuses on photoacoustic tomography, especially improving photoacoustic small-animal imaging performance and applying it to functional deep brain imaging.

Liren Zhu is a PhD candidate at Washington University in St. Louis and a visiting special student at the California Institute of Technology. He received his BS and MS degrees in biomedical engineering from Tsinghua University in 2009 and 2012, respectively. His current research interests include computational imaging, image reconstruction methods, photoacoustic tomography, and compressed ultrafast photography.

Lihong V. Wang earned his PhD from Rice University, Houston, Texas. He currently holds the Bren Professorship of medical engineering and electrical engineering at the California Institute of Technology. He has published 470 peer-reviewed articles in journals and has delivered 460 keynote, plenary, or invited talks. His Google scholar h-index and citations have reached 116 and 56,000, respectively.